nanomaterials

MDPI

Article

Synthesis and Electrochemical Properties of Two-Dimensional RGO/$Ti_3C_2T_x$ Nanocomposites

Changjie Shen [1], Libo Wang [1,*], Aiguo Zhou [1], Bo Wang [2], Xiaolong Wang [1], Weiwei Lian [1], Qianku Hu [1], Gang Qin [1] and Xuqing Liu [3]

1 School of Materials Science and Engineering, Henan Polytechnic University, Jiaozuo 454000, Henan, China; shenchangjie92@163.com (C.S.); zhouag@hpu.edu.cn (A.Z.); wangxiaolong@163.com (X.W.); WWL2116060@163.com (W.L.); hqk@hpu.edu.cn (Q.H.); clqingang@126.com (G.Q.)

2 State Key Laboratory of Solid Lubrication, Lanzhou Institute of Chemical Physics, Chinese Academy of Sciences, Lanzhou 730000, China; bowang@licp.cas.cn

3 School of Materials, University of Manchester, Oxford Road, Manchester M13 9PL, UK; xuqing.liu@manchester.ac.uk

* Correspondence: wanglibo537@hpu.edu.cn; Tel.: +86-0391-3986-910

Received: 16 January 2018; Accepted: 29 January 2018; Published: 31 January 2018

Abstract: MXene is a new type of two-dimensional layered material. Herein, a GO/$Ti_3C_2T_x$ nanocomposite was prepared by a simple liquid phase method, and the obtained GO/$Ti_3C_2T_x$ was transformed into RGO/$Ti_3C_2T_x$ under high temperature with Ar/H_2. The prepared samples were characterized using X-ray diffraction (XRD), Raman measurement, scanning electron microscopy (SEM), energy disperse spectroscopy (EDS), and X-ray photoelectron spectroscopy (XPS). As an electrode material in lithium-ion batteries, the RGO/$Ti_3C_2T_x$ nanocomposite exhibited an excellent electrochemical performance and an excellent rate performance. Compared to pure $Ti_3C_2T_x$, the nanocomposite had a better reversible capacity at different current densities and had no attenuation after 200 cycles, which is one time higher than pure $Ti_3C_2T_x$. The improvement in the specific capacity was due to the excellent electrical conductivity and the unique structure of RGO, in which a charge transfer bridge was built among the $Ti_3C_2T_x$ flakes. Such a bridge shortened the transmission distance of the electrons and ions and effectively controlled the restacking of the laminated materials.

Keywords: MXene; graphene; exfoliation; nanocomposite; lithium-ion battery

1. Introduction

In recent years, two-dimensional (2D) materials have become an important field of research because of their unique properties and have attracted an increasing amount of attention in materials science [1–6]. Graphene-based materials are those that include graphene [7] or graphene-like materials, which have a structure like graphene but contain other elements and compounds. For example, MXene contains $Ti_3C_2T_x$ and Ti_2CT_x [8,9]. MXene are a new kind of layered 2D transition metal carbides and nitrides and are prepared from a MAX phase by Naguib et al. [9] in 2011. The general formula of the MAX phase is $M_{n+1}AX_n$ (n = 1, 2, 3, ...), where M represents transition metal elements (M = Ti, Sr, V, Cr, Ta, Nb, Zr, Mo, and Hf), A represents Group IIIA or IVA elements (A = Al, Ga, In, Ti, Si, Ge, Sn, and Pb) and X represents C or/and N elements [10–12]. The A element is selectively etched from the MAX phase using hydrofluoric acid (HF) [9,13] or a mixture of fluoride salt and hydrochloric acid (HCl) [14] to produce MXene, which are known to possess graphene-like 2D structures. It is more precise to denote these compounds as $M_{n+1}X_n$. Thus far, more than 70 kinds of MAX phase compounds have been reported [15], but until now only the following families have been successfully prepared: Ti_3C_2, Ti_2C, $(Ti_{0.5}Nb_{0.5})_2C$, $(V_{0.5}Cr_{0.5})_3C_2$, Ti_3CN, Ta_4C_3, Nb_2C, V_2C, and Nb_4C_3 [13,16].

Because of their unique structures, MXene has attracted considerable attention in many fields, such as adsorption materials [17–19], lithium-ion batteries [20–26], hydrogen storage materials [27], high capacitor electrode materials [28–32], and additives for polymer composites [33–35].

MXene nanoparticles have a 2D lamellar structure. As the most extensively studied MXene nanomaterial, $Ti_3C_2T_x$ is synthesized by etching Ti_3AlC_2 with hydrofluoric acid or a mixed solution of fluoride salts and hydrochloric acid. MXene nanosheets, owing to the strong van der Waals interaction between adjacent layers, will inevitably self-stack in the drying process. The restacking 2D sheets MXene have a limited electrolyte-accessible surface area, which leads to an insufficient use of the properties of MXene. This problem can be solved by creating an open structure that can provide more space for electrode materials to come into contact with the electrolyte by introducing spacers between the MXene layers, such as carbon nanotubes and graphene [36,37]; combined with other conductive materials, these material can alleviate the restacking and reduce the volume change during the charge/discharge process [38,39]. Liu et al. [40] reported that the Ti_3C_2/CNTs nanocomposite showed a capacity of 428.1 mAh/g at 0.5 C. Liang et al. [41] tested interwoven MXene nanosheets/carbon-nanotube Composites as Li-S cathode hosts, and a stable performance was obtained over long cycles with only 0.043% decay.

In this paper, we report a new method by which an individual $Ti_3C_2T_x$ nanolayer can be obtained. The obtained mixture of GO/$Ti_3C_2T_x$ can be further transformed into an RGO/$Ti_3C_2T_x$ nanocomposite by a simple reduction method under high temperature with Ar/H_2, and using the RGO/$Ti_3C_2T_x$ nanocomposite as the anode in lithium-ion batteries has a much higher electrochemical performance than pure $Ti_3C_2T_x$.

2. Experimental Sections

2.1. Preparation of $Ti_3C_2T_x$

Ti_3AlC_2 is the precursor of $Ti_3C_2T_x$ and was synthesized in our previous report [34]. Ti_3AlC_2 powders were obtained from a mixture of Ti powders, Al powders, and graphite in a molar ratio of 3:1.1:2 (Beijing Xingrongyuan Technology Co. Ltd., Beijing, China), and the mixture of powders was then sintered at 1400 °C for 2 h in an argon atmosphere using a tube furnace (Luoyang shenjia kiln Co. Ltd., Luoyang, China). Then, 5 g of the Ti_3AlC_2 powders (400 mesh, $\leq$37 μm) were immersed in 100 mL of a mixed solution of HCl and LiF and stirred for 48 h at 60 °C. The mixed solution was then centrifuged and washed with deionized water until the supernatant liquid was neutral. Finally, the sample was dried in a vacuum oven at 70 °C for 12 h.

2.2. Preparation of GO/$Ti_3C_2T_x$ and RGO/$Ti_3C_2T_x$ Nanocomposites

GO was synthesized with expanded graphite by a modified Hummers method [42]. Firstly, 0.1 g of GO (a mass ratio of 20%) is dispersed in deionized water and using ultrasound separation for 30 min to spread them evenly. Then, 0.5 g of $Ti_3C_2T_x$ was added to the solution via ultrasonic shock for 30 min until a stable solution was formed, and was kept for 12 h. The obtained sample was frozen with liquid nitrogen and dried using a freeze dryer (BioSafer Technology Co. Ltd., Guangzhou, China). The as-prepared powder was the GO/$Ti_3C_2T_x$ nanocomposite. In order to obtain the RGO/$Ti_3C_2T_x$ nanocomposite, GO/$Ti_3C_2T_x$ was sintered using a tube furnace at 450 °C for 4 h with a mixture of argon (98%) and hydrogen (2%).

2.3. Material Characterization

The crystal structures and morphologies of the samples were measured using X-ray powder diffraction (XRD, Rigaku SmartLab X-ray diffractometer with Cu Kα radiation, accelerating voltage = 40 kV, Tokyo, Japan), scanning electron microscopy (SEM, Merlin Compact, Carl Zeiss NTS GmnH accelerating voltage = 15 kV, Jena, Germany), and energy dispersive spectroscopy (EDS, Oxford instruments Co. Ltd., Oxford, UK). Raman spectra of the powder samples were measured on

a LabRAM HR800 Raman microscope (Edison, NJ, USA) with a laser excitation wavelength of 532 nm. The chemical states of the elements in the samples were characterized using X-ray photoelectron spectroscopy (XPS) on a PHI-5702 multifunctional X-ray photoelectron spectrometer (Perkin–Elmer, Waltham, MA, USA). Mg Kα radiation was used as the excitation source. The binding energies of the target elements were determined with a pass energy of 29.35 eV and a resolution of about 0.3 eV.

2.4. Electrochemical Measurement

To investigate the electrochemical properties of the RGO/$Ti_3C_2T_x$ nanocomposite, experiments were carried out in a standard LIR2016-type coin cell. The working electrodes were made by grind the mixture of 80 wt % sample materials, 10 wt % polyvinylidenefluoride (PVDF), and 10 wt % acetylene black. Then a solution of *N*-methyl-2-pyrrolidone (NMP) was added and stirred for several minutes. Finally, the mixture slurry was coated on Cu foil and dried in a vacuum oven at 110 °C for 12 h. The dried electrode sheets were punched into discs (14 mm) and then assembled into a coin cell in an argon-filled glove box using lithium metal as the cathode electrode, and 1 M $LiPF_6$ solution in a mixture of ethylene carbonate (EC)/dimethyl carbonate(DMC)/ethylmethyl carbonate (EMC) in a 1:1:1 volume ratio was used as the electrolyte. A microporous membrane was used as the separator. The coin cell was tested on a Xinwei battery tester; the electrochemical window was 0.01–3.0 V, and the current densities were 50, 100, 400, 800, and 1000 mA/g. The electrochemical impedance spectroscopy (EIS) was characterized using an electrochemical workstation (Parstat 2273, Princeton, NJ, USA) with a range from 100 kHz to 50 mHz.

3. Results and Discussion

The X-ray diffraction (XRD) patterns of Ti_3AlC_2, $Ti_3C_2T_x$, and GO/$Ti_3C_2T_x$ and RGO/$Ti_3C_2T_x$ nanocomposites are shown in Figure 1a. As seen in the XRD patterns, the characteristic peaks of Ti_3AlC_2 disappeared, while a relatively strong characteristic peak of $Ti_3C_2T_x$ can be found at about 6.5°. After the combination of $Ti_3C_2T_x$ with GO, the characteristic peaks of $Ti_3C_2T_x$ were detected in the GO/$Ti_3C_2T_x$ nanocomposite; the (002) diffraction peak of $Ti_3C_2T_x$ was broader, and the full width at half maximum (FWHM) increased, which means that there was minimal stacking and a random arrangement of $Ti_3C_2T_x$ nanolayers. After heat treatment at high temperature in Ar/H_2, a double peak appeared at small angles in the XRD pattern of RGO/$Ti_3C_2T_x$, and this was mainly attributed to the different inter-layer spacing; the two peaks correspond to $Ti_3C_2T_x$. Meanwhile, a weak peak around $2\theta = 25^\circ$ was observed, indicating that GO nanosheets were reduced to form RGO. Besides the diffraction peaks of $Ti_3C_2T_x$ and RGO, Li_3AlF_6 was also found. In the XRD pattern of pure $Ti_3C_2T_x$, there were no peaks corresponding to Li_3AlF_6. This was because Li_3AlF_6 was hidden between the $Ti_3C_2T_x$ layers and exposed only after the exfoliation of $Ti_3C_2T_x$ into individual nanolayers. The Raman spectra were measured to further confirm the structure and composition of the as-prepared samples. As shown in Figure 1b, compared to pure $Ti_3C_2T_x$, the samples of both GO/$Ti_3C_2T_x$ and RGO/$Ti_3C_2T_x$ had two distinct peaks at 1350 cm^{-1} (D band) and 1590 cm^{-1} (G band), and these findings are consistent with the literature [43]. The results indicate that RGO and $Ti_3C_2T_x$ were successfully combined.

Figure 2a,b shows the scanning electron microscopy (SEM) images of Ti_3AlC_2 and $Ti_3C_2T_x$. It can be clearly seen that $Ti_3C_2T_x$ had a typical layer structure with a broad particle size distribution. The size of the $Ti_3C_2T_x$ particles was on the micrometer scale. The gap between $Ti_3C_2T_x$ nanolayers is about several hundred nanometers. Figure 2c,d are SEM images of the GO/$Ti_3C_2T_x$ and RGO/$Ti_3C_2T_x$ nanocomposites. There were no lamellar-structure microparticles of $Ti_3C_2T_x$, and there was clearly a typical individual flake shape. Additionally, small amounts of nanoparticles were found, and there were Li_3AlF_6 impurities, according to the XRD analysis. The red rectangle and yellow line in Figure 2e represent the surface and linear scanning ranges, respectively, and the results are shown in Figure 2f. The light and dark regions indicate the elemental contents. The region in the lower left corner of the Ti mapping is darker, while in the C mapping it is light, which means that graphene was located at this position. In combination with the linear scanning of Ti and C, the distributions of RGO and $Ti_3C_2T_x$ are

shown in Figure 2e with different colors. From this, it was determined that the multilayers of $Ti_3C_2T_x$ were successfully exfoliated, and the sheets were separated into a single-layer open structure.

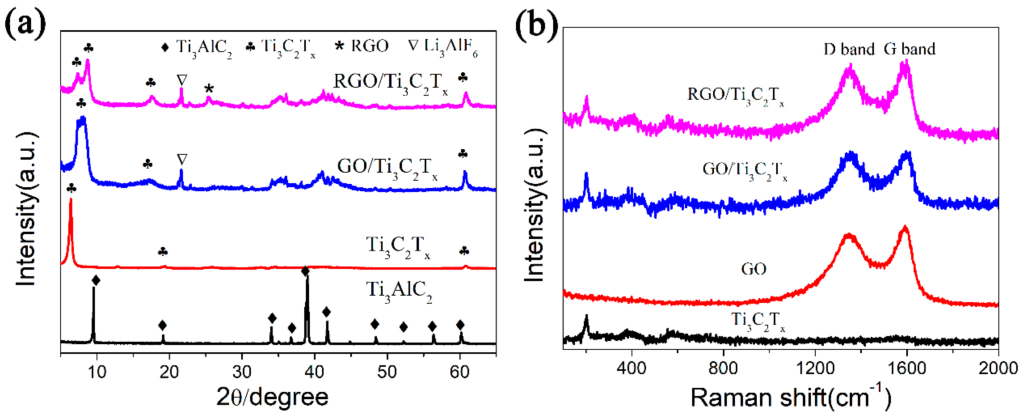

Figure 1. (**a**) X-ray diffraction (XRD) patterns and (**b**) Raman spectrum of Ti_3AlC_2, $Ti_3C_2T_x$, and GO/$Ti_3C_2T_x$, and RGO/$Ti_3C_2T_x$ nanocomposites.

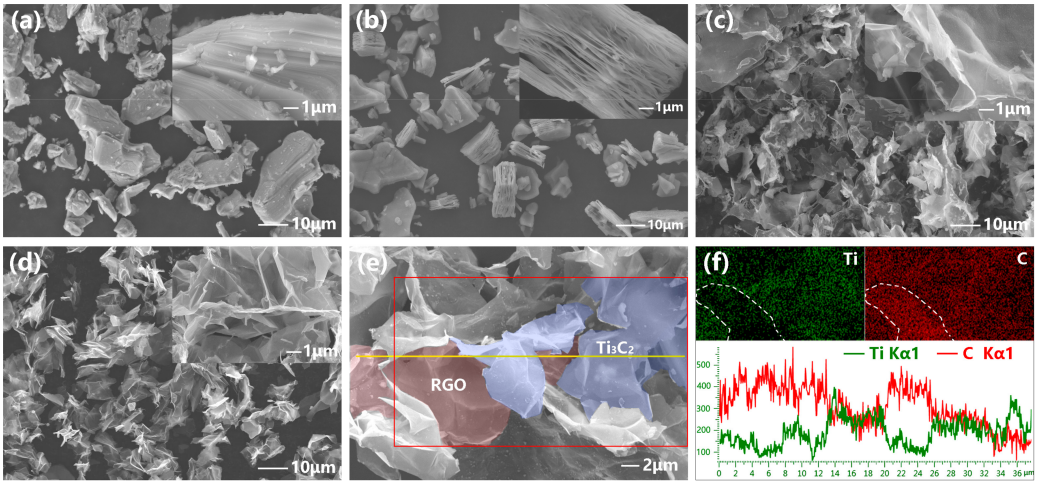

Figure 2. Scanning electron microscopy (SEM) image of Ti_3AlC_2 (**a**), $Ti_3C_2T_x$ (**b**), GO/$Ti_3C_2T_x$ (**c**), and RGO/$Ti_3C_2T_x$ (**d**). Element area profile and linear scanning of RGO/$Ti_3C_2T_x$ (**e**,**f**).

The transmission electron microscopy (TEM) image was used to further characterize the microstructure of the nanomaterials, and the TEM result is shown in Figure 3. As shown in Figure 3a, the layer structure of $Ti_3C_2T_x$ nanosheets has stacked together; in Figure 3b, there is a typical graphene sheet structure. In the TEM image of RGO/$Ti_3C_2T_x$ (Figure 3c), the nanocomposite has been stripped into a more fragile sheet; which is consistent with the SEM results.

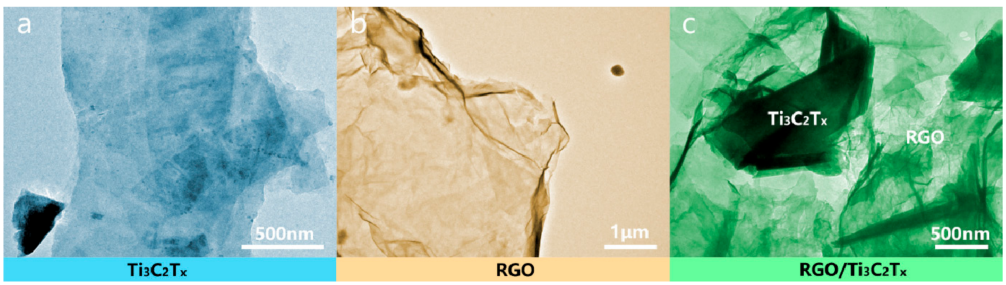

Figure 3. TEM image of $Ti_3C_2T_x$ (**a**), RGO (**b**), and RGO/$Ti_3C_2T_x$ (**c**).

The surface of the RGO/$Ti_3C_2T_x$ nanocomposite was analyzed using X-ray photoelectron spectroscopy (XPS). The survey spectra (Figure 4a) and the high-resolution XPS spectra of Ti2p, C1s, and O1s of the RGO/$Ti_3C_2T_x$ sample are shown in Figure 4b–d. The Ti2p spectrum can be deconvoluted into six peaks corresponding to Ti atoms (455.0, 455.8, and 457.1 eV), Ti–O (458.7 eV), $TiO_{2-x}F_x$ (459.3 eV), and C–Ti–F_x (460.2 eV), and this is consistent with the literature [44]. The C1s XPS spectrum of the RGO/Ti_3C_2 nanocomposite (Figure 4b) was fitted using four peaks. The dominant peak corresponds to the C–C bond, accompanied by three minor peaks at 286.0, 284.2, and 281.5 eV which are assigned to the C=O, C=C, and C–Ti bonds, respectively [45–47]. The O1s peak can be deconvoluted into five symmetrical peaks. The fitting peaks around 529.9, 531.6, 532.0, 532.5, and 533.7 eV are attributed to Ti–O, C–OH, C–Ti–$(OH)_x$, C=O, and O=C–OH [44,48]. The results show that $Ti_3C_2T_x$ and RGO formed a hybrid structure composite, and this is in good agreement with the SEM images and the XRD pattern.

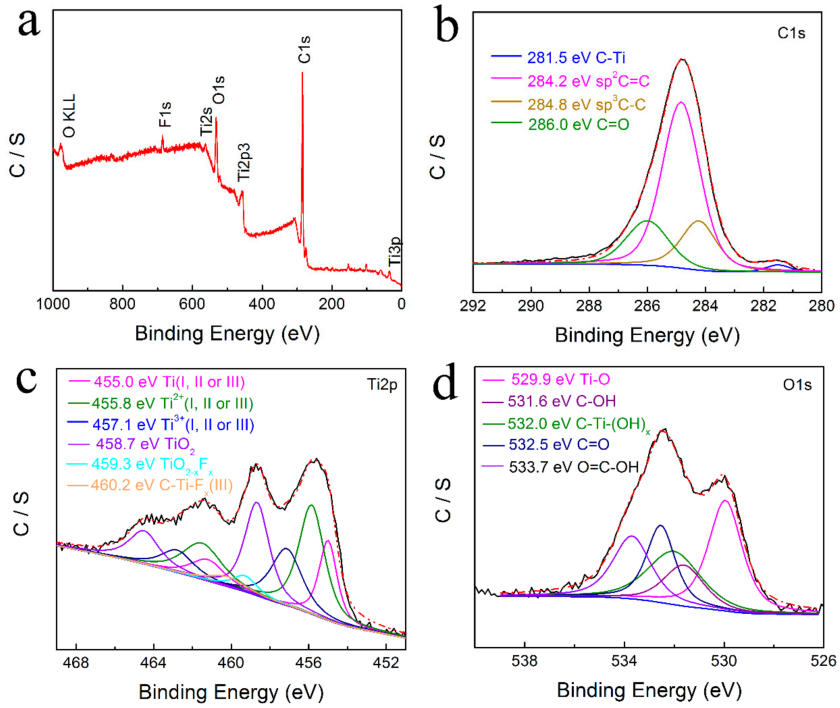

Figure 4. The survey spectrum (**a**) and high-resolution XPS spectra of the C1s (**b**), Ti2p (**c**), and O1s (**d**) peaks of the RGO/Ti_3C_2 nanocomposite.

The electrochemical properties of the RGO/$Ti_3C_2T_x$ nanocomposite were tested using a LIR2016 coin-type cell. Galvanostatic charge-discharge (GCD) cycling and electrochemical impedance spectroscopy (EIS) were also carried out. Specific capacity is usually one of the most important parameters for evaluating the performance of electrode materials. The charge-discharge profiles of $Ti_3C_2T_x$ and the RGO/$Ti_3C_2T_x$ nanocomposite as the activities for lithium-ion battery (LIB) anode at different cycles with a current density of 50 mA/g in the voltage range from 0.01 to 3.0 V (vs. Li^+/Li) are shown in Figure 5, respectively. The first discharge capacities of $Ti_3C_2T_x$ and the RGO/$Ti_3C_2T_x$ nanocomposite are 178 and 364 mAh/g, respectively. The first discharge capacity of the RGO/$Ti_3C_2T_x$ nanocomposite was much higher than the theoretical capacity of $Ti_3C_2T_x$ (~260 mAh/g) [49]. The stabilities and rate performances of $Ti_3C_2T_x$ and the RGO/$Ti_3C_2T_x$ nanocomposites at various current densities are shown in Figure 6. The first charge-discharge coulombic efficiencies for $Ti_3C_2T_x$ and the RGO/$Ti_3C_2T_x$ composite electrodes are 53% and 62%. The irreversible capacity and the low efficiency of the first cycle of the charge-discharge behavior are mainly ascribed to the irreversible electrolyte reduction on the layers of the nanocomposite and

to the formation of a solid electrolyte interface (SEI) [14,50]. In subsequent cycles, the discharge capacities of $Ti_3C_2T_x$ were 98, 82, 65, 55, and 50 mAh/g at current densities of 50, 100, 400, 800, and 1000 mA/g, respectively; for the RGO/$Ti_3C_2T_x$nanocomposite, at the same current densities, the discharge capacities in subsequent cycles were 221, 161, 138, 122, and 111 mAh/g, respectively. These results show that the RGO/$Ti_3C_2T_x$ nanocomposite had better electrochemical performance than $Ti_3C_2T_x$ and benefited from the improved conductivity and the open structure. The open structure increases Li ion access to active sites and connected the layered $Ti_3C_2T_x$ [38,39,51].

In addition, in terms of cycle stability, the results of $Ti_3C_2T_x$ and the RGO/$Ti_3C_2T_x$ nanocomposite at a current density of 500 mA/g for 200 cycles are shown in Figure 7. At the same current density, the RGO/$Ti_3C_2T_x$ nanocomposite had a higher capacity than $Ti_3C_2T_x$; in particular, a specific capacity of 140 mAh/g was obtained, which is much higher than that of pure $Ti_3C_2T_x$ (53 mAh/g). Compared with a previous report on SnO_2-GNS materials [52], the capacity of the RGO/$Ti_3C_2T_x$ material shows almost no attenuation. The columbic efficiencies of $Ti_3C_2T_x$ and the RGO/$Ti_3C_2T_x$ nanocomposite are both close to 100%. In contrast, the RGO/$Ti_3C_2T_x$ nanocomposite had a higher capacity than that of $Ti_3C_2T_x$ at the same current densities. Furthermore, it was also found that, after a number of cycles, the capacity of the RGO/$Ti_3C_2T_x$ nanocomposite increased slowly with cycling. This result was possibly because of the specific structures that had loose morphologies with minimal restacking of $Ti_3C_2T_x$ nanolayers, and this facilitated the electrochemical activation process and improved the electrochemical performance [53].

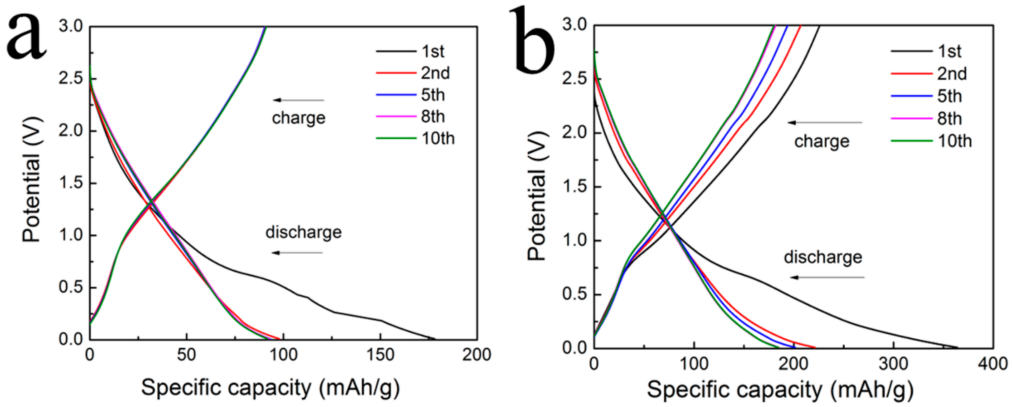

Figure 5. Charge–discharge profiles of (**a**) $Ti_3C_2T_x$ and (**b**) the RGO/$Ti_3C_2T_x$ nanocomposite electrode at different cycles with a current density of 50 mA/g.

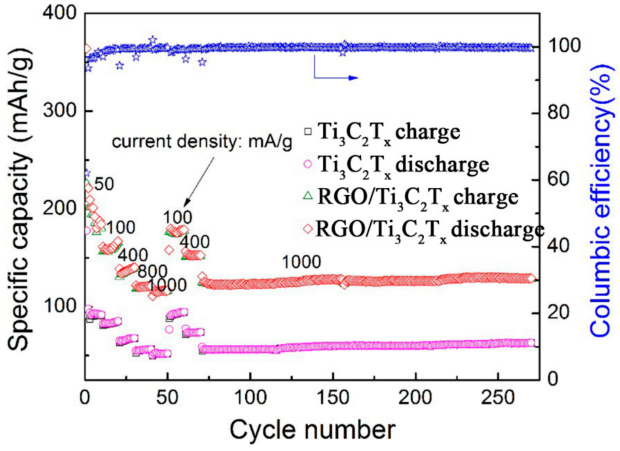

Figure 6. Rate performance of $Ti_3C_2T_x$ and the RGO/$Ti_3C_2T_x$ nanocomposite at different current densities.

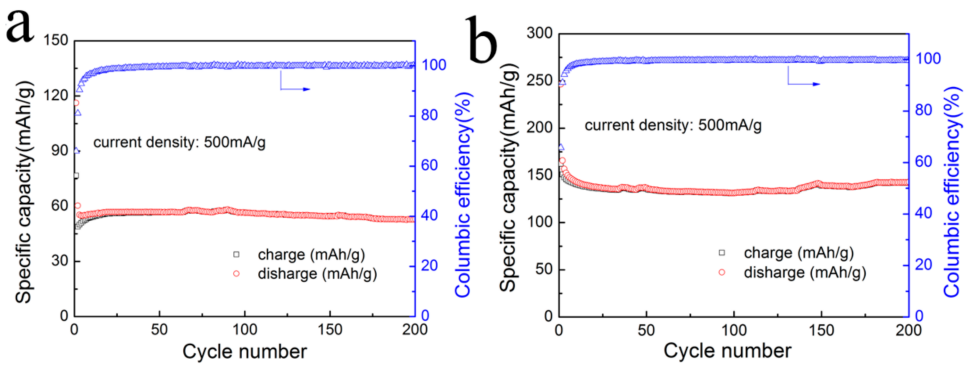

Figure 7. Cycling performance of (**a**) $Ti_3C_2T_x$ and (**b**) the RGO/$Ti_3C_2T_x$ nanocomposite at a current density of 500 mA/g.

Figure 8 shows the cyclic voltammetry (CV) test results of the RGO/$Ti_3C_2T_x$ nanocomposite. In the process of first lithiation, a peak around 0.51 V was observed and was attributed to the formation of a solid electrolyte interphase (SEI) [48]; the peak at 1.69 V was caused by the trapping of Li^+ between the sheets in the electrode materials [23,54]. In the process of delithiation, a peak around 2.15 V was observed and corresponded to the extraction of Li^+ from the layer electrode. From the reported literature [43], in the pure graphene, there was no obvious redox peaks, excluding the reduced peaks at low voltage.

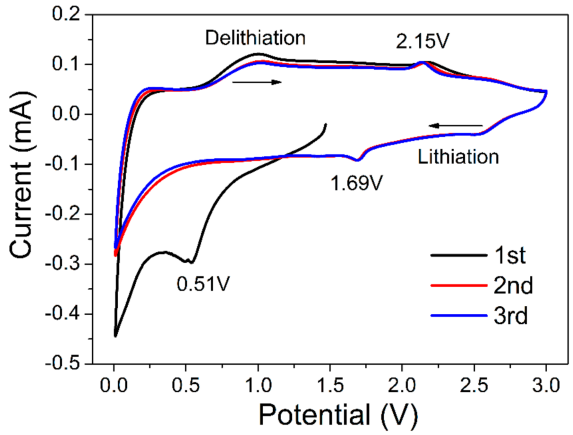

Figure 8. Cyclic voltammetry (CV) curves of the RGO/$Ti_3C_2T_x$ nanocomposite from 3.0 to 0.01 V at a scan rate of 0.2 mV/s.

The EIS of $Ti_3C_2T_x$ and RGO/$Ti_3C_2T_x$ are shown in Figure 9. The EIS spectrum consists of a semi-circle and a sloped line. The formation of the semi-circle was attributed to the movement of the lithium ions and to the charge transfer through the SEI films [12,40]. The diameter of the semi-circle was related to the charge transfer resistance at the electrode. Comparing the Nyquist plots of the two different samples, the RGO/$Ti_3C_2T_x$ nanocomposite had a relatively small semicircular diameter, which indicates that the RGO/$Ti_3C_2T_x$ nanocomposite had a much lower charge transfer resistance than pure $Ti_3C_2T_x$. This was mainly attributed to the addition of RGO, which provided many effective conductive pathways and improved the electron transfer between the $Ti_3C_2T_x$ flakes. Additionally, the exfoliation of 2D $Ti_3C_2T_x$ materials effectively increased the contact area between $Ti_3C_2T_x$ and the electrolyte, which may decrease resistance and promote electron transfer. Finally, the hybrid structure provided more active fresh sites or Li ion diffusion channels. The above analyses from the electrochemical tests confirmed that the RGO/$Ti_3C_2T_x$ nanocomposite has excellent reversibility and rate stability.

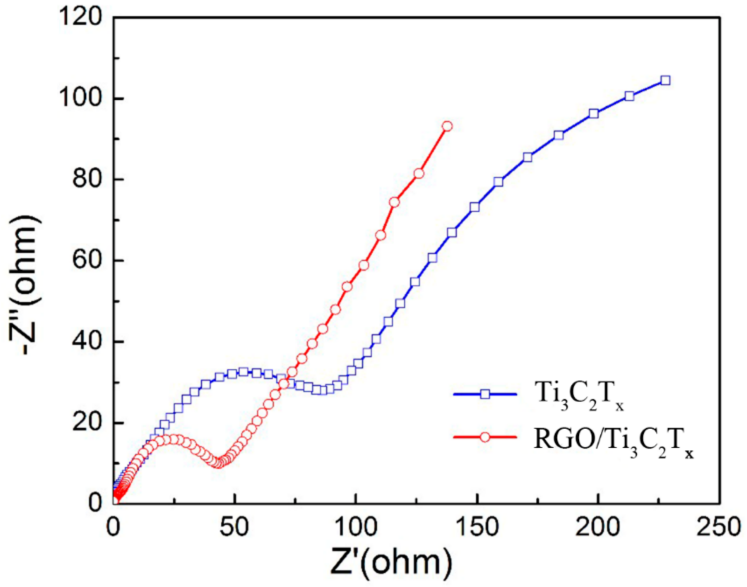

Figure 9. Electrochemical impedance spectroscopy (EIS) plots of the $Ti_3C_2T_x$ and RGO/$Ti_3C_2T_x$.

4. Conclusions

In this study, 2D/2D RGO/$Ti_3C_2T_x$ nanocomposites were successfully prepared using a simple method and was used as an electrode in lithium-ion batteries. The RGO/$Ti_3C_2T_x$ nanocomposite had a hybrid structure and exhibited better performance than pure $Ti_3C_2T_x$. In the nanocomposite, RGO helped develop paths for fast electron transport, in which a charge transfer bridge was built among the $Ti_3C_2T_x$ flakes. Such a bridge shortened the transmission distance of the electrons and ions and effectively controlled the restacking of the laminated materials. Furthermore, the RGO/$Ti_3C_2T_x$ nanocomposite exhibited a stable capacity of 125 mAh/g and maintained a relatively high coulomb efficiency at a current density of 1000 mA/g for 200 cycles.

Acknowledgments: This research was supported by the National Nature Science Foundation of China (51772077, 51472075, 51403056), the Plan for Scientific Innovation Talent of Henan Province (134100510008), the Scientific and Technological Project of Henan Province (172102210284), and the Program for the Innovative Research Team of Henan Polytechnic University (T2013-4).

Author Contributions: Libo Wang and Aiguo Zhou conceived and designed the experiments; Changjie Shen, Xiaolong Wang, and Weiwei Lian performed the experiments; Bo Wang and Xuqing Liu analyzed the data; Qianku Hu and Gang Qin contributed reagents/materials/analysis tools; Changjie Shen wrote the paper.

Conflicts of Interest: The authors declare no conflict of interest.

References

1. Jing, Y.; Zhou, Z.; Cabrera, C.R.; Chen, Z. Graphene, inorganic graphene analogs and their composites for lithium ion batteries. *J. Mater. Chem. A* **2014**, *2*, 12104–12122. [CrossRef]
2. Naguib, M.; Gogotsi, Y. Synthesis of two-dimensional materials by selective extraction. *Acc. Chem. Res.* **2015**, *48*, 128–135. [CrossRef] [PubMed]
3. Kuila, T.; Bose, S.; Mishra, A.K.; Khanra, P.; Kim, N.H.; Lee, J.H. Chemical functionalization of graphene and its applications. *Prog. Mater. Sci.* **2012**, *57*, 1061–1105. [CrossRef]
4. Politano, A.; Chiarello, G. Plasmon modes in graphene: Status and prospect. *Nanoscale* **2014**, *6*, 10927–10940. [CrossRef] [PubMed]
5. Ferrari, A.C.; Bonaccorso, F.; Fal'ko, V. Science and technology roadmap for graphene, related two-dimensional crystals, and hybrid systems. *Nanoscale* **2015**, *7*, 4598–4810. [CrossRef] [PubMed]
6. Gugliuzza, A.; Politano, A.; Drioli, E. The advent of graphene and other two-dimensional materials in membrane science and technology. *Curr. Opin. Chem. Eng.* **2017**, *16*, 78–85. [CrossRef]

7. Li, D.; Kaner, R.B. Graphene-based materials. *Science* **2008**, *320*, 1170–1171. [CrossRef] [PubMed]
8. Naguib, M.; Mashtalir, O.; Carle, J.; Presser, V.; Lu, J.; Hultman, L.; Gogotsi, Y.; Barsouum, M.W. Two-Dimensional Transition Metal Carbides. *ACS Nano* **2012**, *6*, 1322–1331. [CrossRef] [PubMed]
9. Naguib, M.; Kurtoglu, M.; Presser, V. Two-Dimensional Nanocrystals Produced by Exfoliation of Ti_3AlC_2. *Adv. Mater.* **2011**, *23*, 4248–4253. [CrossRef] [PubMed]
10. Tang, Q.; Zhou, Z.; Shen, P. Are MXenes promising anode materials for Li ion batteries? Computational studies on electronic properties and Li storage capability of Ti_3C_2 and $Ti_3C_2X_2$ (X = F, OH) monolayer. *J. Am. Chem. Soc.* **2012**, *134*, 16909–16916. [CrossRef] [PubMed]
11. Barsoum, M.W. The $M_{N+1}AX_N$ Phases: A New Class of Solids: Thermodynamically Stable Nanolaminates. *Prog. Solid State Chem.* **2000**, *28*, 201–281. [CrossRef]
12. Gao, Y.; Wang, L.; Li, Z. Electrochemical performance of Ti_3C_2 supercapacitors in KOH electrolyte. *J. Adv. Ceram.* **2015**, *4*, 130–134. [CrossRef]
13. Naguib, M.; Mochalin, V.N.; Barsoum, M.W.; Gogotsi, Y. 25th anniversary article: MXenes: a new family of two-dimensional materials. *Adv. Mater.* **2014**, *26*, 992–1005. [CrossRef] [PubMed]
14. Zhang, H.; Dong, H.; Zhang, X.; Xu, Y.; Fransaer, J. Cu_2O Hybridized Titanium Carbide with Open Conductive Frameworks for Lithium-ion Batteries. *Electrochim. Acta* **2016**, *202*, 24–31. [CrossRef]
15. Shein, I.R.; Ivanovskii, A.L. Graphene-like nanocarbides and nanonitrides of *d* metals (MXenes): Synthesis, properties and simulation. *Micro Nano Lett.* **2013**, *8*, 59–62. [CrossRef]
16. Lei, J.-C.; Zhang, X.; Zhou, Z. Recent advances in MXene: Preparation, properties, and applications. *Front. Phys.* **2015**, *10*, 276–286. [CrossRef]
17. Fard, A.K.; Mckay, G.; Chamoun, R.; Rhadfi, T.; Preud'Homme, H.; Atieh, M.A. Barium removal from synthetic natural and produced water using MXene as two dimensional (2-D) nanosheet adsorbent. *Chem. Eng. J.* **2017**, *317*, 331–342. [CrossRef]
18. Mashtalir, O.; Cook, K.M.; Mochalin, V.N.; Crowe, M.; Barsoum, M.W.; Gogotsi, Y. Dye adsorption and decomposition on two-dimensional titanium carbide in aqueous media. *J. Mater. Chem. A* **2014**, *2*, 14334–14338. [CrossRef]
19. Peng, Q.; Guo, J.; Zhang, Q.; Xiang, J.; Liu, B.; Zhouo, A.; Liu, R.; Tian, Y. Unique lead adsorption behavior of activated hydroxyl group in two-dimensional titanium carbide. *J. Am. Chem. Soc.* **2014**, *136*, 4113–4116. [CrossRef] [PubMed]
20. Lashgari, H.; Abolhassani, M.R.; Boochani, A.; Elahi, S.M.; Khodadadi, J. Electronic and optical properties of 2D graphene-like compounds titanium carbides and nitrides: DFT calculations. *Solid State Commun.* **2014**, *195*, 61–69. [CrossRef]
21. Er, D.; Li, J.; Naguib, M.; Gogotsi, Y.; Shenoy, V.B. Ti_3C_2 MXene as a high capacity electrode material for metal (Li, Na, K, Ca) ion batteries. *ACS Appl. Mater. Interfaces* **2014**, *6*, 11173–11179. [CrossRef] [PubMed]
22. Mashtalir, O.; Naguib, M.; Mochalin, V.N.; Dall'Agnese, Y.; Heon, M.; Barsoum, M.W.; Gogotsi, Y. Intercalation and delamination of layered carbides and carbonitrides. *Nat. Commun.* **2013**, *4*, 1716–1722. [CrossRef] [PubMed]
23. Naguib, M.; Come, J.; Dyatkin, B.; Presser, V.; Taberna, P.-L.; Simon, P.; Barsoum, M.W.; Gogotsi, Y. MXene: a promising transition metal carbide anode for lithium-ion batteries. *Electrochem. Commun.* **2012**, *16*, 61–64. [CrossRef]
24. Anasori, B.; Xie, Y.; Beidaghi, M.; Lu, J.; Hosler, B.C. Two-Dimensional, Ordered, Double Transition Metals Carbides (MXenes). *ACS Nano* **2015**, *9*, 9507–9516. [CrossRef] [PubMed]
25. Lukatskaya, M.R.; Mashtalir, O.; Ren, C.E.; Dall'Agnese, Y.; ROzier, P.; Taberna, P.L.; Naguib, M.; Simon, P.; Barsoum, M.W.; Gogotsi, Y. Cation intercalation and high volumetric capacitance of two-dimensional titanium carbide. *Science* **2013**, *341*, 1502–1505. [CrossRef] [PubMed]
26. Khazaei, M.; Arai, M.; Sasaki, T. OH-terminated two-dimensional transition metal carbides and nitrides as ultralow work function materials. *Phys. Rev. B* **2015**, *92*, 075411–075421. [CrossRef]
27. Hu, Q.; Sun, D.; Wu, Q.; Wang, H.; Wang, L.; Liu, B.; Zhou, A.; He, J. MXene: A new family of promising hydrogen storage medium. *J. Phys. Chem. A* **2013**, *117*, 14253–14260. [CrossRef] [PubMed]
28. Ling, Z.; Rena, C.E.; Zhao, M.-Q.; Yang, J.; Giammarco, J.M.; Qiu, J.; Barsoum, M.W.; Gogotsi, Y. Flexible and conductive MXene films and nanocomposites with high capacitance. *PNAS* **2014**, *111*, 16676–16681. [CrossRef] [PubMed]

29. Rakhi, R.B.; Ahmed, B.; Hedhili, M.N.; Anjum, D.H.; Alshareef, H.N. Effect of Postetch Annealing Gas Composition on the Structural and Electrochemical Properties of Ti_2CT_x MXene Electrodes for Supercapacitor Applications. *Chem. Mater.* **2015**, *27*, 5314–5323. [CrossRef]
30. Hu, M.; Li, Z.; Zhang, H.; Hu, T.; Zhang, C.; Wu, Z.; Wang, X. Self-assembled $Ti_3C_2T_x$ MXene film with high gravimetric capacitance. *Chem. Commun.* **2015**, *51*, 13531–13533. [CrossRef] [PubMed]
31. Lin, S.-Y.; Zhang, X. Two-dimensional titanium carbide electrode with large mass loading for supercapacitor. *J. Power Sources* **2015**, *294*, 354–359. [CrossRef]
32. Wang, L.; Zhang, H.; Wang, B.; Shen, C.; Zhang, C.; Hu, Q.; Zhou, A.; Liu, B. Synthesis and electrochemical performance of $Ti_3C_2T_x$ with hydrothermal process. *Electron. Mater. Lett.* **2016**, *12*, 702–710. [CrossRef]
33. Huang, Z.; Wang, S.; Kota, S.; Pan, Q.; Barsoum, M.W.; Li, C.Y. Structure and crystallization behavior of poly(ethylene oxide)/$Ti_3C_2T_x$ MXene nanocomposites. *Polymer* **2016**, *102*, 119–126.
34. Zhang, H.; Wang, L.; Chen, Q.; Li, P.; Zhou, A.; Cao, X.; Hu, Q. Preparation, mechanical and anti-friction performance of MXene/polymer composites. *Mater. Des.* **2016**, *92*, 682–689. [CrossRef]
35. Zhang, H.; Wang, L.; Zhou, A.; Shen, C.; Dai, Y.; Liu, F.; Chen, J.; Li, P.; Hu, Q. Effects of 2-D transition metal carbide Ti_2CT_x on properties of epoxy composites. *RSC Adv.* **2016**, *6*, 87341–87352. [CrossRef]
36. Mashtalir, O.; Lukatskaya, M.R.; Zhao, M.-Q.; Barsoum, M.W.; Gogotsi, Y. Amine-Assisted Delamination of Nb_2C MXene for Li-Ion Energy Storage Devices. *Adv. Mater.* **2015**, *27*, 3501–3506. [CrossRef] [PubMed]
37. Boota, M.; Anasori, B.; Voigt, C.; Zhao, M.-Q.; Barsoum, M.W.; Gogotsi, Y. Pseudocapacitive Electrodes Produced by Oxidant-Free Polymerization of Pyrrole between the Layers of 2D Titanium Carbide (MXene). *Adv. Mater.* **2015**, *28*, 1517–1522. [CrossRef] [PubMed]
38. Zhao, C.; Wang, Q.; Zhang, H. Two-Dimensional Titanium Carbide/RGO Composite for High-Performance Supercapacitors. *ACS Appl. Mater. Interfaces* **2016**, *8*, 15661–15667. [CrossRef] [PubMed]
39. Xu, S.; Wei, G.; Li, J. Flexible MXene—graphene electrodes with high volumetric capacitance for integrated co-cathode energy conversion/storage devices. *J. Mater. Chem. A* **2017**, *5*, 17442–17451. [CrossRef]
40. Liu, Y.; Wang, W.; Ying, Y.; Wang, Y.; Peng, X. Binder-free layered Ti_3C_2/CNTs nanocomposite anodes with enhanced capacity and long-cycle life for lithium-ion batteries. *Dalton Trans.* **2015**, *44*, 7123–7126. [CrossRef] [PubMed]
41. Liang, X.; Rangom, Y.; Kwok, C.Y.; Pang, Q.; Nazar, L.F. Interwoven MXene Nanosheet/Carbon-Nanotube Composites as Li-S Cathode Hosts. *Adv. Mater.* **2016**, *29*. [CrossRef] [PubMed]
42. Dreyer, D.R.; Park, S.; Bielawski, C.W. The chemistry of graphene oxide. *Chem. Soc. Rev.* **2010**, *39*, 228–240. [CrossRef] [PubMed]
43. Shan, H.; Li, X.; Cui, Y. Sulfur/Nitrogen Dual-doped Porous Graphene Aerogels Enhancing Anode Performance of Lithium Ion Batteries. *Electrochim. Acta* **2016**, *205*, 188–197. [CrossRef]
44. Halim, J.; Cook, K.M.; Naguib, M.; Eklund, P.; Gogotsi, Y.; Rosen, J.; Barsoum, M.W. X-ray photoelectron spectroscopy of select multi-layered transition metal carbides (MXenes). *Appl. Surf. Sci.* **2016**, *362*, 406–417. [CrossRef]
45. Dong, Y.; Pang, H.; Ren, S.; Chen, C.; Cji, Y.; Yu, T. Etching single-wall carbon nanotubes into green and yellow single-layer graphene quantum dots. *Carbon* **2013**, *64*, 245–251. [CrossRef]
46. Lyth, S.M.; Shao, H.; Liu, J. Hydrogen adsorption on graphene foam synthesized by combustion of sodium ethoxide. *Int. J. Hydrog. Energy* **2014**, *39*, 376–380. [CrossRef]
47. Wang, Y.-S.; Yang, S.-Y.; Li, S.-M.; Tien, H.-W.; Hsiao, S.-T.; Liao, W.-H.; Liu, C.-H.; Chang, K.-H.; Ma, C.-C.M.; Hu, C.-C. Three-dimensionally porous graphene—carbon nanotube composite-supported PtRu catalysts with an ultrahigh electrocatalytic activity for methanol oxidation. *Electrochim. Acta* **2013**, *87*, 261–269.
48. Wang, G.; Xing, W.; Zhuo, S. Nitrogen-doped graphene as low-cost counter electrode for high-efficiency dye-sensitized solar cells. *Electrochim. Acta* **2013**, *92*, 269–275. [CrossRef]
49. Sun, D.; Wang, M.; Li, Z. Two-dimensional Ti_3C_2 as anode material for Li-ion batteries. *Electrochem. Commun.* **2014**, *47*, 80–83. [CrossRef]
50. Luo, J.; Tao, X.; Zhang, J.; Xia, Y.; Huang, H.; Zhang, L.; Gan, Y.; Liang, C.; Zhang, W. Sn^{4+} Ion Decorated Highly Conductive Ti_3C_2 MXene: Promising Lithium-Ion Anodes with Enhanced Volumetric Capacity and Cyclic Performance. *ACS Nano* **2016**, *10*, 2491–2499.
51. Ren, C.E.; Zhao, M.-Q.; Makaryan, T.; Gogotsi, Y. Porous Two-Dimensional Transition Metal Carbide (MXene) Flakes for High-Performance Li-Ion Storage. *ChemElectroChem* **2016**, *3*, 689–693. [CrossRef]

52. Deng, Y.; Fang, C.; Chen, G. The developments of SnO_2/graphene nanocomposites as anode materials for high performance lithium ion batteries: A review. *J. Power Sources* **2016**, *304*, 81–101. [CrossRef]
53. Du, F.; Tang, H.; Pan, L.; Zhang, T.; Lu, H.; Xiong, J.; Yang, J.; Zhang, C. Environmental Friendly Scalable Production of Colloidal 2D Titanium Carbonitride MXene with Minimized Nanosheets Restacking for Excellent Cycle Life Lithium-Ion Batteries. *Electrochim. Acta* **2017**, *235*, 690–699. [CrossRef]
54. Come, J.; Naguib, M.; Rozier, P.; Barsoum, M.W.; Gogotsi, Y.; Taberna, P.-L.; Morcorette, M.; Simon, P. A Non-Aqueous Asymmetric Cell with a Ti_2C-Based Two-Dimensional Negative Electrode. *J. Electrochem. Soc.* **2012**, *159*, A1368–A1373. [CrossRef]